Journal of Physics: Conference Series

PAPER • **OPEN ACCESS**

Normalization in dynamic speckle analysis for non-destructive monitoring of speed of processes

To cite this article: Elena Stoykova *et al* 2021 *J. Phys.: Conf. Ser.* **2091** 012002

Journal of Physics: Conference Series **2091** (2021) 012002 doi:10.1088/1742-6596/2091/1/012002

Normalization in dynamic speckle analysis for non-destructive monitoring of speed of processes

Elena Stoykova, Dimana Nazarova, Lian Nedelchev, Mikhail Levchenko, Nataliya Berberova-Buhova and Branimir Ivanov

Institute of Optical Materials and Technologies - Bulgarian Academy of Sciences, Acad. Georgi Bonchev street, Bl.109, Sofia 1113, Bulgaria

E-mail: elena.stoykova@gmail.com

Abstract. The paper is dedicated to analysis of normalized intensity-based pointwise algorithms for processing dynamic speckle images with spatially varying speckle statistics in non-destructive visualization of regions of faster or slower changes across an object. Both existing and newly proposed algorithms are analyzed. Extraction of speed of changes is done by acquiring correlated in time speckle images formed on the object surface under laser illumination. The studied algorithms have been applied to simulated low and high contrast speckle data. Their performance has been compared to processing of binary patterns as another approach for dealing with varying speckle statistics in the acquired images. The efficiency of the algorithms have been checked on the experimental data, including data in a compressed format. We have proven that the algorithms with normalization at successive instants by a sum of two intensities or a single intensity outperform as a whole the algorithms which apply the time-averaged estimates of the mean value and the variance of speckle intensity.

1. Introduction

Speed of a process, which leads to micro-changes of topography or a refractive index of an object, is encoded in temporal variation of speckle patterns formed on the object surface under laser illumination [1,2]. Dynamic laser speckle, called also biospeckle in some applications, has been used for non-destructive testing of industrial or biological objects. Monitoring of blood flow perfusion in human tissues [3-5], seeds viability [6,7], plants growing and leaves contamination with chemical agents [8,9], and penetration of cosmetic ingredients in human skin [10], analysis of ear biometrics [11] and bacterial response [12,13], study of animal reproduction [14], food assessment [15-17], drying of paints, coatings and polymer thin films [18,19] have been reported.

Usage of a two-dimensional (2D) optical sensor enables pointwise application of Dynamic Speckle Analysis (DSA), which yields speed distribution in space as a 2D map of a statistical parameter. The intensity-based 2D DSA relies on a comparatively large number of correlated in time speckle images to produce a single 2D map of activity for visualizing regions of faster or slower intensity fluctuations across the objects. This DSA implementation has serious advantages as simplicity of the acquisition set-up, high spatial resolution and spatial analysis applicable to 3D objects. The main challenge of the 2D DSA is the speckle nature of the raw data. The small size of speckle grains in the acquired images results in strong spatial intensity fluctuations within the recorded patterns. The relevant information is buried in signal-dependent noise, and the choice of the processing algorithm is crucial. The algorithm is expected to be fast and robust at non-uniform illumination and to provide a weakly fluctuating estimate for constant speed of changes. Another substantial issue in the 2D DSA is storage, transfer and processing of huge amount of data for monitoring a process when a sequence of activity maps is built in time. This makes necessary compression of the speckle data and raises the question of the efficiency of the algorithms in processing compressed data.

We focus in this work on normalization approaches for processing data with spatially varying speckle statistics. A typical example of such statistics is acquisition of speckle images under non-uniform illumination. Both existing and newly proposed algorithms are analyzed. We compared performance of the analysed algorithms by processing simulated and experimental data.

2. Normalized processing

2.1. Description of the raw data

For the intensity-based dynamic speckle measurement, a CMOS or a CCD camera records speckle images of size $N_x \times N_y$ pixels at a pixel interval Δ and a time interval Δt between the frames. This time interval should ensure recording of correlated patterns. Exposure time is small to avoid speckle averaging during the recording. The dynamic range of the camera is adjusted to the dynamic range of the recorded data. The raw data usually are 8-bit encoded intensity images. An object on a vibration-insulated table is illuminated by the linearly polarized laser light. The illuminating beam is spatially filtered, expanded and collimated. Nevertheless, the intensity may be different at its centre and periphery. This results in speckle statistics which varies not only in time but also in space. The non-normalized processing encounters difficulties in correct detection of activity, and some normalization is required.

A 2D activity map is built from *N* speckle images. The input data for a pointwise processing algorithm are sequences $I_{ik,1}, I_{ik,2}..I_{ik,N}; i = 1...N_x, k = 1...N_y$ where $I_{ik,n}$ is the intensity at pixel $(i\Delta, k\Delta)$ and instant $n\Delta t$. The activity estimate is obtained by averaging within the time interval, $T = N\Delta t$. Temporal correlation function, $R_{ik}(\tau)$, where $\tau = m\Delta t$ is the time lag between the compared intensities and $m \geq 0$ is an integer, characterizes intensity fluctuations at pixel $(i\Delta, k\Delta)$. The width of $R_{ik}(\tau)$ gives the temporal correlation radius $\tau_c(i\Delta, k\Delta)$. For non-uniform illumination, the variance of intensity fluctuations, σ_{ik}^2, in $R_{ik}(\tau) = \sigma_{ik}^2 \rho_{ik}(\tau)$ varies from point to point; $\rho_{ik}(\tau)$ is the normalized correlation function respectively.

To check the performance of different normalized algorithms, we generated speckle patterns for a synthetic object consisting of four rectangular regions Z1, Z2, Z3 and Z4 of the same size with temporal correlation radii of intensity fluctuations equal to 10 Δt, 20 Δt, 40 Δt and 80 Δt respectively (figure 1a). Simulation was based on producing correlated wrapped phase distributions in the plane of the object that were propagated to the sensor plane through the objective lens. A 2D array of random delta-correlated phase values uniformly distributed from 0 to 2π was used as an initial phase, and normal distribution was accepted for the phase change in time due to normal movement of the scattering centres with respect to the surface. Mutual independence was accepted for the amplitudes and phases of the scattered light at each scattering centre and between the centres. We used $\rho_{ik}(\tau) = \exp\{-\tau / \tau_c(i\Delta, k\Delta)\}$ for description of the modelled processes. The standard deviation of the phase change between successive images was $\sigma_\varphi = N(0,1)\left[\dfrac{\Delta t}{\tau_c(i\Delta, k\Delta)}\right]^{1/2}$. Speckle integration by the camera pixels was also taken into account. Simulation procedure is described in more details in [20]. We generated speckle patterns of size 256×256 pixels for both low and high contrast speckle at wavelength 532 nm for uniform and non-uniform illumination. A Gaussian intensity distribution $I_0(i\Delta, k\Delta) = I_0 \exp\{-\alpha(i\Delta, k\Delta)\}$ where $I_0 = const$ and $\alpha(i\Delta, k\Delta) = \dfrac{(i-128)\Delta^2 + (k-128)\Delta^2}{\Omega^2}$ with $\Omega = 210\Delta$ is used for simulation. The histograms of intensity fluctuations across the object and the speckle patterns for the simulated four cases are given in figure 1(b) and figure 1(c). At uniform illumination, the speckle statistics is the same in the areas Z1, Z2, Z3 and Z4 and is described by symmetric or asymmetric intensity distributions depending on the contrast. Speckle has the same statistics in the areas of higher or lower activity, and averaging in time is required to visualize these areas. At non-uniform illumination, the histograms of intensity in the acquired patterns become asymmetric both for the low and the high contrast due to darker areas in the acquired images.

2.2. Normalized processing of a test object

A standard approach to deal with non-uniform illumination is to normalize using the estimates of the variance or standard deviation of temporal intensity fluctuations at each point. Besides the normalized temporal correlation function [21]:

$$\hat{C}(i,k,m) \equiv \hat{C}(i\Delta, k\Delta, m\Delta t) = \frac{1}{N\hat{\upsilon}_{ik}} \sum_{n=1}^{N-m} \left(I_{ik,n+m} - \hat{I}_{ik}\right)\left(I_{ik,n} - \hat{I}_{ik}\right) \quad (1)$$

where $\hat{\upsilon}_{ik} = N^{-1} \sum_{n=1}^{N} \left(I_{ik,n} - \hat{I}_{ik}\right)^2$ and $\hat{I}_{ik} = N^{-1} \sum_{n=1}^{N} I_{ik,n}$ are the estimates of the variance and the average intensity at point $(i\Delta, k\Delta)$, effective evaluation of activity is provided by the normalized estimates of the structure function, $\hat{S}_1$, and modified structure function, $\hat{S}_2$, as follows [20,21]:

$$\hat{S}_1(i,k,m) = \frac{1}{N\hat{\upsilon}_{ik}} \sum_{n=1}^{N-m} \left(I_{ik,n+m} - I_{ik,n}\right)^2 \quad , \quad \hat{S}_2(i,k,m) = \frac{1}{N\hat{\upsilon}_{ik}^{1/2}} \sum_{n=1}^{N-m} \left|I_{ik,n+m} - I_{ik,n}\right| \quad (2)$$

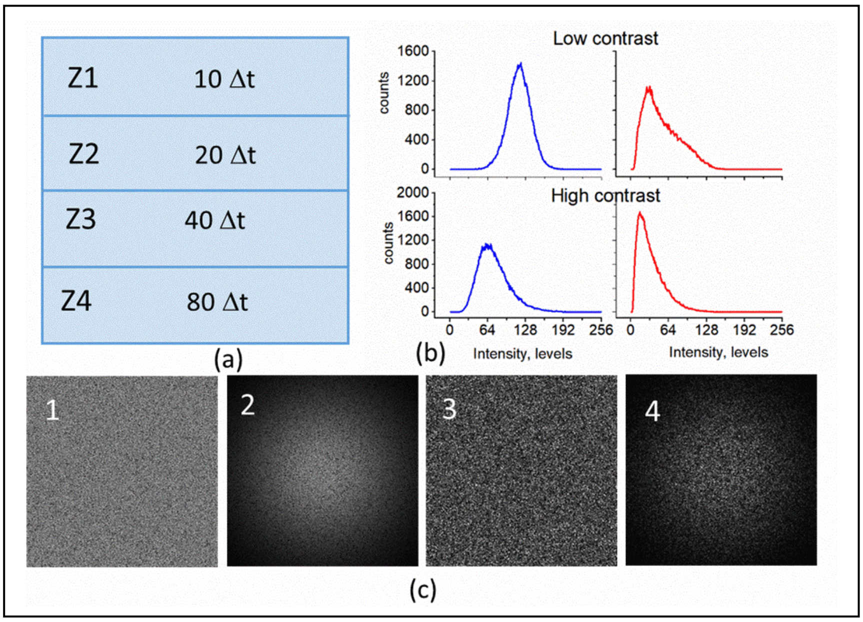

Figure 1. Synthetic object with 4 activity regions Z1, Z2, Z3, Z4 with temporal correlation radii of intensity fluctuations equal to 10Δt, 20Δt, 40Δt and 80Δt (a), speckle intensity histograms (b) for patterns (c) obtained for the object at low contrast and uniform (1) and non-uniform (2) illumination and high contrast and uniform (3) and non-uniform (4) illumination; wavelength 532nm, image size 256×256 pixels.

The need to evaluate the average value and the variance from the sequences of intensity values at all pixels, however, complicates these algorithms. Computation of the variance, $\hat{\upsilon}_{ik}$, by averaging in time is reliable at comparatively high ratios between the acquisition time

$T = N\Delta t$ and the correlation radius, τ_c. In general, the 2D distribution $\hat{\upsilon}_{ik}, i=1...N_x, k=1...N_y$ may strongly differ from $\sigma_{ik}, i=1...N_x, k=1...N_y$. Instead of using $\hat{\upsilon}_{ik}$, one may take the average intensity value or its square for normalization. Efficiency of such an approach was studied in [22].

More flexible algorithms can be built by time-averaging of a fraction whose nominator and denominator are composed from one or two intensity values acquired at different instants. We checked efficiency of several estimates $\hat{S}_l(i,k,m) = (N-m)^{-1}\sum_{n=1}^{N-m} f_{ik,n}^l(m)$ with $f_{ik,n}^3(m) = \frac{I_{ik,n}}{I_{ik,n+m}}$, $f_{ik,n}^4(m) = \left|\frac{I_{ik,n}}{I_{ik,n+m}} - 1\right|$, $f_{ik,n}^5(m) = \left|\frac{I_{ik,n} - I_{ik,n+2m}}{I_{ik,n+m}}\right|$, $f_{ik,n}^6(m) = \frac{|I_{ik,n} - I_{ik,n+m}|}{I_{ik,n} + I_{ik,n+m}}$, $f_{ik,n}^7(m) = \left|\frac{I_{ik,n}}{I_{ik,n+m}} - \frac{I_{ik,n+m}}{I_{ik,n}}\right|$. The estimate $\hat{S}_6$ was proposed earlier [22]; $\hat{S}_6(m=1)$ coincides with Fuji's algorithm [3]. All estimates $\hat{S}_{1-7}$ increase at higher activity and are equal to 0 at zero activity with exception of $\hat{S}_3$ which is equal to 1 in the latter case.

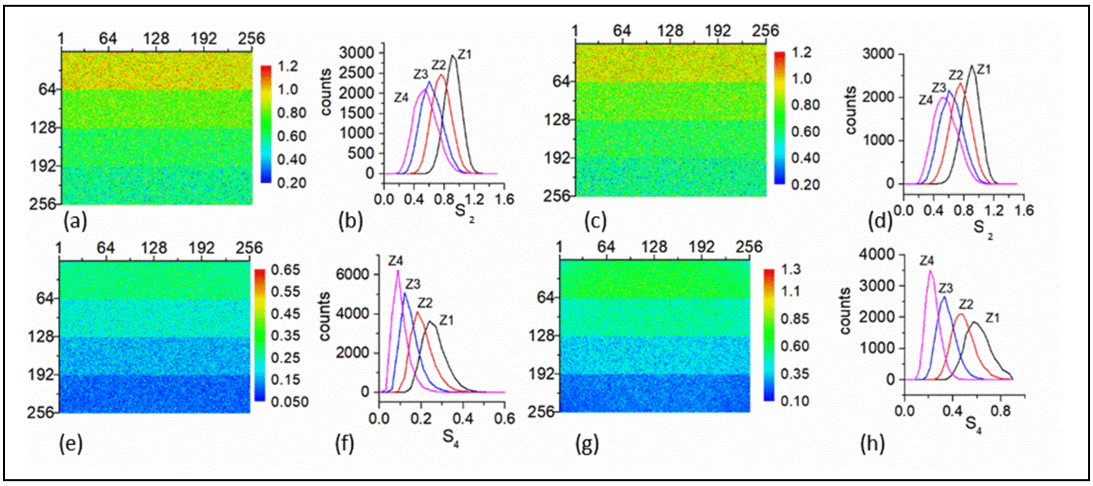

Figure 2. Activity maps for a synthetic object with 4 activity regions Z1, Z2, Z3, Z4 (a,c,e,g) and the histograms of the estimates in these regions (b,d,f,h) for estimates $\hat{S}_2$ (a,b,c,d) and $\hat{S}_4$ (e,f,g,h); (a,b,e,f) - low contrast speckle, (c,d,g,h) - high contrast speckle; N = 256, wavelength 532 nm, m = 10.

We applied the algorithms $\hat{S}_{1-7}$ to a sequence of 256 speckle images with low and high contrast under non-uniform illumination at 532 nm. The exemplary images taken from the processed sequences are given as images 2 and 4 in figure 1(c). The time lag was taken equal to 10Δt. For illustration, we presented in figure 2 the activity maps obtained for $\hat{S}_2$ and $\hat{S}_4$. The four regions of different activity are clearly seen for both estimates. The contrast of the map corresponding to $\hat{S}_4$ seems better, especially for the regions Z3 and Z4 of lower activity. This is understandable in view that accuracy of determination of the variance estimate, $\hat{\upsilon}_{ik}$, in these regions is rather low at $T\tau_c^{-1}$ equal to 6.4 and 3.2 respectively. The large number of entries in each region (256×64) makes possible evaluation of the probability density function of the estimate at a given activity. The histograms of $\hat{S}_2$ and $\hat{S}_4$ for the four activity regions are also shown in figure 2. As is seen, due to strong fluctuations of the estimates, the histograms are rather wide and overlap. The greater the overlap, the lower the sensitivity of the algorithm. For $\hat{S}_{3-7}$, the higher the activity, the wider the histogram. The result is opposite for $\hat{S}_{1-2}$ due to usage of the variance estimate determined at decreasing accuracy when activity goes to a lower level.

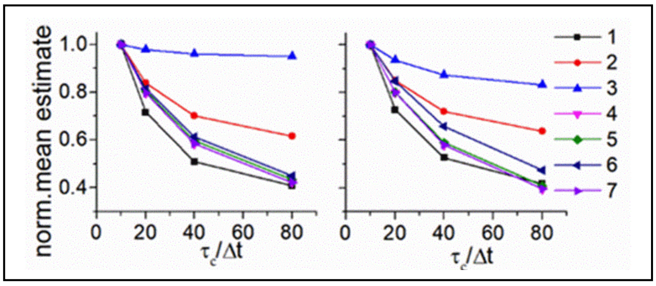

Figure 3. Mean values of the estimates $\hat{S}_{1-7}$ normalized to the mean values in Z1, as a function of the temporal correlation radius; left – low contrast, right – high contrast; *N* = 256, wavelength 532 nm, *m* = 10.

The mean values of the estimates $\hat{S}_{1-7}$ normalized to the mean value for the highest activity in Z1, are shown in figure 3. The mean values as well as the locations of the maximal frequency counts in the histograms depend on activity. As expected, the smallest decrease compared to the value in Z1 is observed for $\hat{S}_3$. This is the fastest algorithm, and despite the low contrast of the map it provided, it can be used for monitoring of objects with large variation of activity across their surface. The largest decrease corresponds to $\hat{S}_1$. The fall of the mean values, when activity is decreasing, is practically the same for the algorithms, $\hat{S}_{4-6}$. They show rather close behavior to $\hat{S}_1$.

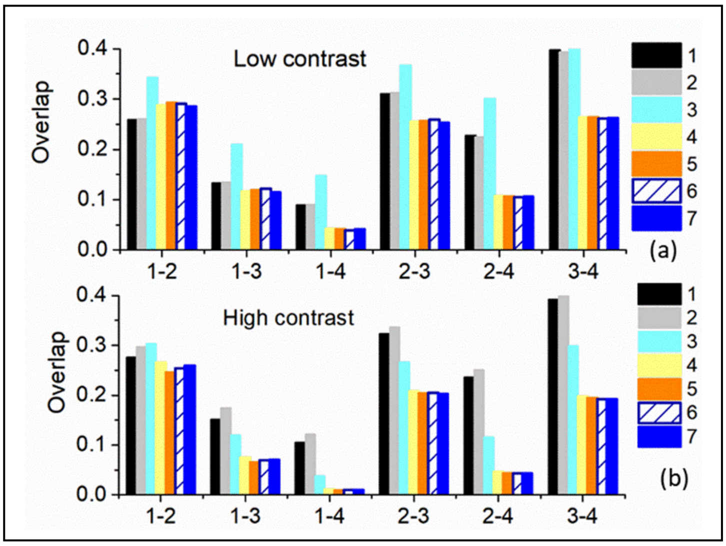

Figure 4. Overlap of histograms of the estimates for activity regions Z1, Z2, Z3, Z4; (1-2) gives the overlap between the histograms in Z1 and Z2, (1-3) – between Z1 and Z3 etc.; *N* = 256, wavelength 532 nm, *m* = 10.

More important parameter for quantitative characterization of sensitivity of the algorithms is the area of overlap of two histograms as a fraction of the total number of entries in a single histogram [20]. Both compared histograms have the same number of entries, and, in our case, it is equal to 256×64. The smaller the overlap, the higher the sensitivity of the algorithms. The overlap as a fraction of 256×64 entries for all algorithms $\hat{S}_{1-7}$ in the cases of low and high contrast speckle is shown in figure 4. The most interesting are the groups of results denoted as 1-2, 2-3 and 3-4 that show comparison of estimates in adjacent spatial regions for the considered test object. The results in the group 1-2 correspond to two spatial areas with close values of the correlation radii – 10 Δt and 20 Δt. For the low contrast case, the results for the algorithms $\hat{S}_{1-2}$ are better than $\hat{S}_{4-7}$ in the group 1-2 , but the result is opposite for the high contrast case. As expected, performance of the algorithm $\hat{S}_3$ is the worst in all cases. Comparison of the estimates for evaluation of activity at τ_c equal to 20Δt and 40Δt (group 2-3) or 40Δt and 80Δt (group 3-4) proves that the algorithms $\hat{S}_{4-7}$ slightly outperform the algorithms $\hat{S}_{1-2}$. They substantially outperform $\hat{S}_{1-2}$ for detection of a high activity area with respect to the low activity area (groups of results 1-3, 1-4 and 2-4). Taking in view the additional advantage of faster computation, these algorithms can be a preferable choice for processing speckle data with spatially varying statistics.

Effective solution for visualization of activity for speckle data with spatially varying statistics is processing of binary patterns [23]. The mean intensity value, $\hat{I}_{ik}$, at each point $(i\Delta, k\Delta)$, can be used as a threshold for binarization. Sequences are formed as $\vartheta_{ik,n} = \pm 1, n = 1,2...N$ depending on $I_{ik,n}$ value being less or larger than $\hat{I}_{ik}$. A polar correlation function is calculated as:

$$\hat{P}(i,k,m) = (N-m)^{-1} \sum_{n=1}^{N-m} \vartheta_{ik,n} \vartheta_{ik,n+m} \tag{3}$$

Contrary to the estimates, $\hat{S}_{1-7}$, the polar correlation function gets a lower value at higher activity. For the test object in figure 1, we obtained the following values for the overlap between the histograms corresponding to the four different activities: 0.2894 (0.3067) for Z1 and Z2, 0.1757 (0.2013) and 0.1248 (0.1484) for Z1 compared to Z3 and Z4 respectively, 0.3446 (0.3592) for Z2 and Z3, 0.2703 (0.2915) for Z2 and Z4 and 0.4140 (0.4175) for Z3 and Z4. The values in the brackets correspond to the high contrast case. As is seen, this estimator exhibits similar behaviour as the normalized structure and modified structure functions.

3. Processing of experimental data

For experimental verification of the algorithms, we chose a specially designed circular metal object composed from flat annular regions with alternating depths (0 and -2 mm) with respect to the upper surface. There are two flat regions at zero depth and two hollow regions - a central circular section and an annular region. Different activity on the object surface was created by evaporation of polyester paint, which covered the object to form a flat layer. In this way, the hollow regions contained larger quantity of paint compared to the flat surface of the other two annular regions. The object was positioned on a vibration-insulated table and illuminated with a linearly polarized light from a He-Ne laser at 632.8 nm. The drying of the paint produced a dynamic speckle. The speckle images were recorded as 8-bit encoded bitmap images by a color CMOS camera X06c-s (manufactured by Baumer) at interval Δt = 250 ms between the frames. The size of the captured images was 780 × 582 pixels. A single image occupied 1.29 MB, the exposure time was 100 μs.

An exemplary speckle image in bitmap format is shown in figure 5(a). As is seen, the intensity distribution is not uniform within the image. The regions of different activity are in practice indistinguishable. We compared normalized processing provided by $\hat{S}_1$, $\hat{S}_2$ and $\hat{S}_4$. The maps of the estimates after processing 256 patterns for a time lag equal to 10Δt are presented in figure 5 (b-d). Despite the comparatively long sequence of images, the estimate $\hat{\upsilon}_{ik}$ introduces additional fluctuations in $\hat{S}_1$ and $\hat{S}_2$ and in their maps respectively. This decreases the sensitivity of both estimators. Usage of non-normalized structure and modified structure function provides smoother maps at the expense of erroneous determination of activity due to the non-uniformity of illumination. The algorithm $\hat{S}_4$ gives an activity map with enhanced contrast. Evaluation of the processing time on MatLab shows that building a map of size 600×582 pixels for $\hat{S}_1$ and $\hat{S}_2$ requires about 3 times more time than computing of the map of $\hat{S}_4$.

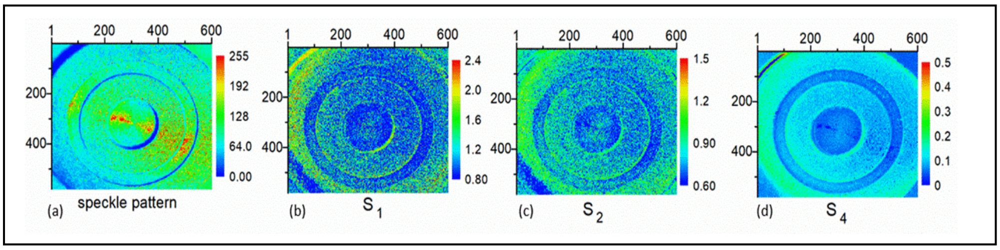

Figure 5. Speckle pattern acquired for a circular metal object with annular regions of different depths in a bitmap format (a) and activity maps for $\hat{S}_1$ (b), $\hat{S}_2$ (c) and $\hat{S}_4$ (d); $N = 256$, wavelength 632.8 nm, $m = 10$.

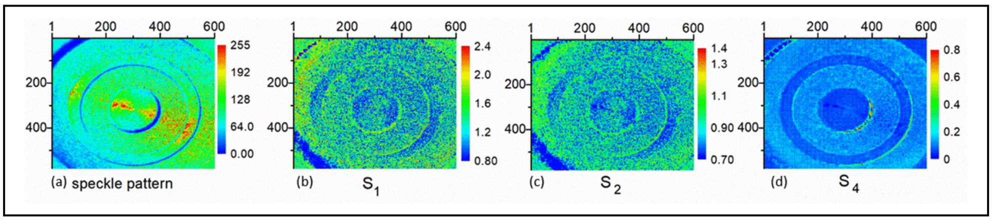

Figure 6. Speckle pattern acquired for a circular metal object with annular regions of different depths in a JPEG format (a) and activity maps for $\hat{S}_1$ (b), $\hat{S}_2$ (c) and $\hat{S}_4$ (d); $N = 256$, wavelength 632.8 nm, $m = 10$.

Storage of big data arrays for monitoring of processes entails usage of data compression. For the intensity-based DSA implementation, we have recently proposed binarization or coarse quantization of the acquired images [23,24]. Another solution is to store the data in the JPEG format. A speckle image decompressed from a JPEG image stored at quality parameter equal to 70 is shown in figure 6(a). Actually, this is the same image as that in figure 5(a). The size of a single image in the JPEG format is 60.4 KB. The results of processing 256 decompressed JPEG images by using $\hat{S}_1$, $\hat{S}_2$ and $\hat{S}_4$ are presented in figure 6(c-d). The contrast of the maps for the normalized structure and modified structure functions is not very good. However, the result provided by $\hat{S}_4$ is acceptable because the regions of different activity are clearly visualized. The only drawback is an artefact expressed as a regular grid of slightly higher values of the estimate. This grid related to the JPEG compression scheme is obscured in the maps in figure 6(b) and figure 6(c) due to different normalization. Since the presence of the grid does not interfere with characterization of activity, one may conclude that JPEG compression is applicable for the DSA data.

In summary, we have studied normalization in intensity-based DSA for processing raw speckle data with spatially varying statistics, as e.g. under non-uniform illumination. We analysed the existing correlation-based algorithms in which normalization is done by using the estimate of the variance at each point. We proposed and studied modifications of algorithms which use for normalization at a given instant a sum of two intensities or a single intensity. We checked efficiency of the algorithms by applying them to low and high contrast simulated data and also compared them for processing of binary patterns as another approach for dealing with varying speckle statistics in the acquired images. The efficiency of the algorithms have been checked for processing experimental data, including data in a compressed format. We have proven that the pointwise algorithms in which normalization is done at each instant by using one or two intensity values are more efficient than the algorithms applying the time-averaged estimates of the mean value and the variance of speckle intensity.

Acknowledgements.
The reported study was funded by the National Science Fund of Bulgaria (contract КП-06-Russia/7). E. Stoykova thanks European Regional Development Fund within the Operational Programme "Science and Education for Smart Growth 2014–2020" under the Project CoE "National center of Mechatronics and Clean Technologies" BG05M2OP001-1.001-0008. M. Levchenko thanks 2020 Plenoptic Imaging H2020 Marie Sklodowska-Curie Innovative Training Network, project No 956770.

References

[1] Goodman J 2007 *Speckle Phenomena in Optics: Theory and Applications* (Roberts and Company Publishers)
[2] Rabal H J and Braga R A Jr 2009 *Dynamic Laser Speckle and Applications* (CRC Press).
[3] Fujii H, Nohira K, Yamamoto Y, Ikawa H and Ohura T 1987 *Appl. Opt.* **26** 5321–5
[4] Serov A and Lasser T 2005 *Opt. Express* **13** 6416–28
[5] Rajan V, Varghese B, van Leeuwen T and Steenbergen W 2006 *Opt. Lett.* **31** 468–70
[6] Braga R, Fabbro I, Borem F, Rabelo G, Arizaga R, Raba H andTrivi M 2003 *Biosystems Eng.* **86**, 287-94
[7] Braga R, Rabelo G, Granato L, Santos E, Machado J, Arizaga R, Rabal H and Trivi M 2005 *Biosystems Eng.* **91** 465-9
[8] Braga R A, Dupuy L, Pasqual M and Cardoso R R 2009 *Eur.Biophys. J.* **38** 679–86
[9]. Ivanov B, Stoykova E, Berberova N, Nikova T, Krumov E and Malinowski N 2013 *Bulg. Chem. Commun.* **45** 149 – 53
[10] Stoykova E, Blagoeva B, Nazarova D, Nedelchev L, Nikova T, Berberova N, Kim , and Kang H 2018 *Opt. Quant.Electron.* **50** 191-201
[11] Chatterjee A, Singh P, Bhatia V and Prakash S 2019 *Opt. Las.Technol.*, **112** 368-78
[12]. Murialdo S E, Sendra G H, Passoni L I, Arizaga R, Gonzalez J F, Rabal H and Trivi M 2009 *J. Biomed. Opt.* **14** 064015
[13]. Mandracchia B, Palpacuer J, Nazzaro F, Bianco V, Rega R, Ferraro P 2018 *IEEE J. Selected Topics in Quant. Electron.* **25** 1-6
[14]. Macedo R, Barreto Filho J, Braga R Jr, Rabelo G 2009 *Reprod. Fertil. Dev.* **22** 170–1
[15]. Ansari M Z, Minz P D and Nirala A K 2012 *Proc. IEEE Conf.on Recent Advances in Information Technology* (IEEE) 873–6
[16]. Mulone C, Budini N, Vincitorio F, Freyre C, López Díaz A and Ramil Rega O 2013 *Proc. SPIE* **8785**, 87851X
[17]. Lyubenova T, Stoykova E, Nacheva E, Ivanov B, Panchev I and Sainov V 2013 *Proc. SPIE* **8770**, 87700S
[18] Harizanova R, Gaydarov V, Zamfirova G, Stoykova E, Nazarova D, Blagoeva B and Nedelchev L 2019 *Thin Solid Films* **68**7 137441
[19]. Martí-López L, Cabrera H, Martínez-Celorio R A and González-Peña R 2010 *Opt. Commun*. **283** 4972-7
[20] Stoykova E, Nazarova D, Berberova N and Gotchev A 2015 Opt. Express 23 25128-42
[21] Stoykova E, Ivanov B, Nikova T 2014 *Opt. Lett*. **39** 115-8
[22] Stoykova E 2018 *Proc. SPIE* **10834**, 108341O
[23] Stoykova E, Kang H, Kim Y, Nazarova D, Nedelchev L, Ivanov B, Berberova N and Mateev G 2018 *Opt. Las. Eng.* **111** 50-57
[24] Stoykova E, Nazarova D, Nedelchev L, Ivanov B, Blagoeva B, Oh K and Park J 2020 *Appl. Opt.* **59** 2810-19